IEEE Access
Multidisciplinary ⋮ Rapid Review ⋮ Open Access Journal

Received December 5, 2021, accepted December 21, 2021, date of publication January 14, 2022, date of current version February 3, 2022.

Digital Object Identifier 10.1109/ACCESS.2022.3143544

A Miniature Flexible Coil for High-SNR MRI of the Pituitary Gland

JIAHAO LIN[1,2], (Member, IEEE), SIYUAN LIU[2], MARVIN BERGSNEIDER[3], J. ROCK HADLEY[4], GIYARPURAM N. PRASHANT[5], SOPHIE PEETERS[3], ROBERT N. CANDLER[2,6], (Senior Member, IEEE), AND KYUNGHYUN SUNG[1], (Member, IEEE)

[1]Department of Radiological Sciences, University of California at Los Angeles, Los Angeles, CA 90095, USA
[2]Department of Electrical and Computer Engineering, University of California at Los Angeles, Los Angeles, CA 90095, USA
[3]Department of Neurosurgery, University of California at Los Angeles, Los Angeles, CA 90095, USA
[4]Department of Radiology, The University of Utah, Salt Lake City, UT 84132, USA
[5]Department of Neurosurgery, Thomas Jefferson University, Philadelphia, PA 19107, USA
[6]California NanoSystems Institute, Los Angeles, CA 90095, USA

Corresponding author: Siyuan Liu (siyuanliu@g.ucla.edu)

This work was supported in part by the DGSOM Seed Grant Program Award (The Spitzer Grant Research Program), and in part by the American Association of Neurological.

This work involved human subjects or animals in its research. Approval of all ethical and experimental procedures and protocols was granted by the Institutional Review Board (IRB), and performed in compliance with the United States Health Insurance Portability and Accountability Act (HIPAA) of 1996.

ABSTRACT Clinical magnetic resonance imaging (MRI) of the pituitary gland sometimes fails to detect small pituitary tumors due to limited signal-to-noise ratio (SNR) and spatial resolution. Thus, neurosurgeons may need to resort to surgical exploration and systematic slicing of the pituitary gland to identify the small pituitary tumors. In this work, we designed a single-loop miniature flexible coil that can be surgically positioned millimeters from the pituitary gland, enabling high-SNR pituitary MRI. We investigated the spatial distributions of the image SNR of the miniature coil, via both numerical simulation and phantom experiments. We also explored the feasibility of increased SNR within the pituitary gland based on simulated surgical placements. Compared to the commercial head coil, our miniature coil achieved up to a 19-fold SNR improvement within the region of interest, and the simulation and phantom experiment reached a good agreement, with an error of $1.1\% \pm 0.8\%$. High resolution MRI scans further demonstrated the visual improvement of the miniature coil against the commercial head coil. The cross-validation of the simulation and the phantom experiment showed the potential of using the numerical simulation model to accelerate the coil design prototyping and iteration and to optimize coil design in the future.

INDEX TERMS Flexible RF-coil, miniature, coil simulation, pituitary microadenomas, signal-to-noise ratio, high-resolution, endoscopic endonasal surgery.

I. INTRODUCTION

There is a strong clinical need to improve the resolution of magnetic resonance imaging (MRI) for the detection of small pathological lesions. A salient example is Cushing's disease (CD): a potentially fatal disorder caused by an adrenocorticotropin hormone (ACTH)-producing pituitary tumor. While the median size of pituitary tumors (microadenomas) causing CD is 5 mm [1], a significant percentage is less than 3 mm in size [2]. Currently, 3T MRI is unable to detect up to 50% of microadenomas in CD [3]–[6]. This failure of diagnostic imaging thwarts the primary and optimal treatment of CD: surgical excision of the offending tumor. In such cases without an imaging-identifiable tumor, neurosurgeons must consider surgically ''exploring'' the anterior pituitary gland by making multiple parallel incisions typically spaced 2-3 mm apart with the hope of fortuitously encountering the tumor. In addition to the real possibility of not finding a tumor, this technique adds the risk of permanently damaging the normal gland.

Standard 3T pituitary MRI protocols generate multi-slice 2-dimensional (2D) images with a typical in-plane resolution of 0.7×0.7 mm^2 and a through-plane slice thickness of 3 mm [7]. When considering various shapes of the pituitary gland, partial volume averaging, and motion-related degradation [8], it is not surprising that MR images with an in-plane pixel size of 0.7 mm commonly fail to detect lesions smaller than 3 mm.

One of the common factors limiting MRI spatial resolution is signal-to-noise ratio (SNR). Two approaches for increased

The associate editor coordinating the review of this manuscript and approving it for publication was Yi Zhang.

SNR are to use higher strengths (e.g., 7T MRI scanner [9], [10]) and to design application-specific radiofrequency (RF) coil arrays. These two are generally additive when combined with each other. Advancements have been made with flexible RF coil arrays. Conforming the coil elements to the patient's surface anatomy achieves higher SNR in directly adjacent regions, which unfortunately is of limited value for pituitary imaging given that the pituitary gland is located centrally within the cranium. Another approach to improve SNR is to place a separate receive-only RF coil in close proximity to the imaging target [11]. One example in clinical use, the endorectal coil designed for prostate imaging [12], has had limited use due to patient discomfort related to the relatively large diameter of the endorectal component. Chittiboina *et al.* [13] adopted the endorectal prostate coil for pituitary imaging. The study demonstrated a potential 10-fold increase in SNR by positioning the coil apparatus within the sphenoid sinus via a sublabial approach in a cadaver [13]. However, the design included a potential concern that the coil is needed to be positioned blindly, given the complete obstruction of the surgical corridor by the probe.

In this study, we report our initial evaluation of this novel coil design using a custom-built phantom which allowed us to precisely measure SNR. We designed a single loop miniature flexible coil that could easily be placed via one nostril and optimally situated within the sphenoid sinus under direct endoscopic visualization (Fig. 1). Our coil design shares the same clinical implementation limitation as to the previous study [13], in that it must be used as part of an elective surgical operation with the aim of removal of the tumor. The ideal orientation of the coil is parallel to the orientation of the main magnetic field, B_0. As the surgical positioning for endoscopic surgery is supine, our investigations of sphenoid sinus anatomy revealed that this coil orientation may not be anatomically possible in some cases. We therefore designed the phantom to allow us to study the effect of coil angulation relative to the B_0 field [14], [15]. The specific aims of our study are to 1) investigate spatial distributions of the image SNR for various coil rotation angles (θ) using a numerical simulation model and phantom experiments, and 2) test the feasibility of increased SNR within the pituitary gland based on simulated surgical placement results. The miniature coil was tested with high-resolution imaging to confirm its visual improvement against the commercial head coil. The coil design was iteratively developed by utilizing numerical electromagnetic simulations, and this cross-validation approach will be useful in further optimizing the coil in the future, including the potential select an optimal coil from a predetermined range of coil shapes and sizes.

II. MATERIALS AND METHODS

A. DESIGN OPTIMIZATION RELATED TO SURGICAL PLACEMENT RESTRICTIONS AND SPHENOID SINUS DIMENSIONS

From a coil design perspective, the coil diameter should not only be large enough to provide sufficient coverage for pituitary MRI but must also fit within the physical spatial constraint of the sphenoid sinus. Specifically, the diameter of the coil needs to be large enough - larger than the pituitary - such that the pituitary is in the region of high sensitivity. The diameter also needs to be large enough to achieve sensitivity at a depth of the farthest point of the pituitary because the optimal coil diameter is proportional to the imaging depth of interest: $R_{optimal} = \frac{d_{max}}{\sqrt{5}}$, where d_{max} is the maximum distance of interest from the coil [16]. Endonasal placement requires that the coil be able to bend slightly beyond a U-shape in order to pass by the nostril. In 20 consecutive endoscopic pituitary surgeries, various sizes of sterile cotton patties (''cottonoids'') were subjectively assessed by author MB. The experience revealed that a coil diameter up to 2.5-cm could easily be inserted without hyperangulation (kinking). Once past the nostril, further advancement into the sphenoid sinus was easy and safe.

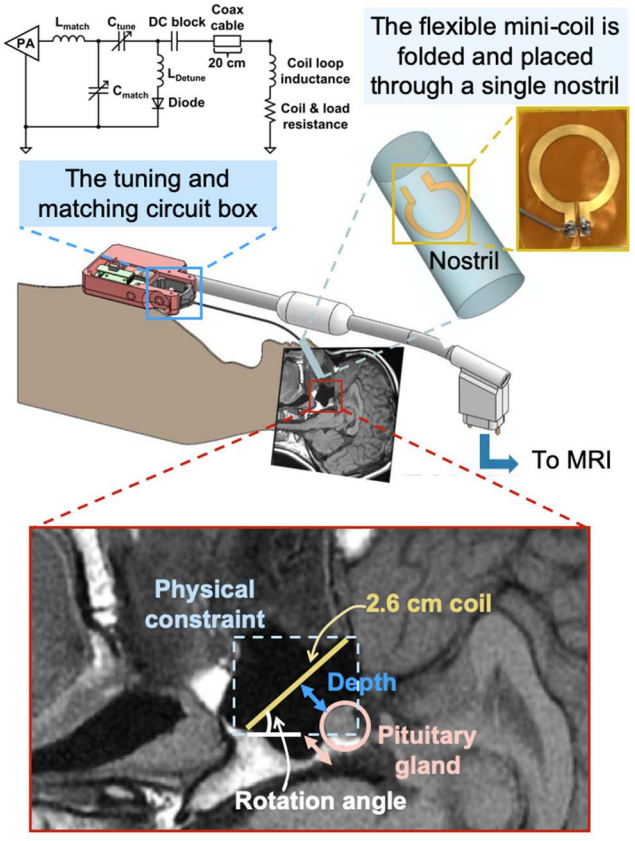

FIGURE 1. Coil design and its surgical placement. The miniature coil is built on a flexible printed circuit board and connected to the tune and match box, which allows fine-tuning and matching of the coil remotely. The local pituitary coil is placed against the pituitary gland, and the coil rotation angle is defined as the angle between the coil plane and the scanner bed.

B. COIL AND INTERFACE DESIGN

The coil (Fig. 1) consisted of a 20 mm inner diameter loop made from a single continuous copper trace (3 mm in width and 17.8 μm in thickness) on a flexible printed circuit board (PCB). A coaxial cable (Siemens Healthineers, Forchheim,

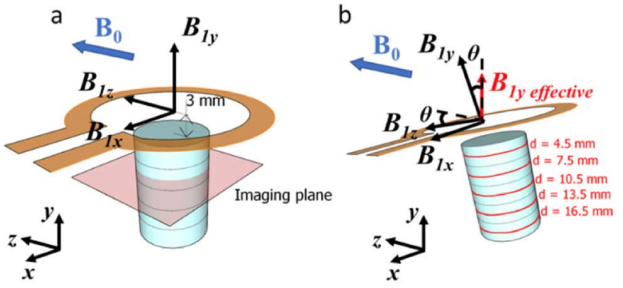

FIGURE 2. Schematic diagram of the miniature coil. The blue cylinders represent the region of interest (ROI) at various distances d from the coil. B_0 is in the +z axis. A: The coil resides in the x-z plane at $\theta = 0°$. B: The coil is rotated around the x-axis at an angle, θ, where: $0° < \theta \leq 90°$.

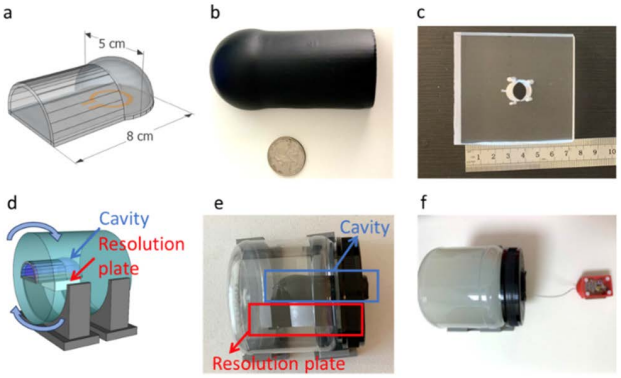

FIGURE 3. Experimental setup, including the igloo cavity, resolution plate, and agar phantom. An igloo cavity holds the coil and is sealed to hold only air, mimicking the sinus cavity. A resolution plate is placed directly on the outside of the igloo cavity to measure the SNR at the location where the pituitary gland would be. Outside of the igloo is surrounded by agar gel to act as a phantom a: CAD model of the igloo cavity. The coil was placed inside the cavity. b: The 3D-printed igloo cavity. The cavity was waterproofed with the Plasti Dip (Plasti Dip Int., Minneapolis, MN, USA). A U.S. quarter is shown for reference. c: The resolution plate with hole diameters 1 mm, 1.6 mm, 2 mm, 2.4 mm, 2.8 mm, and 12.7 mm. The smaller holes were used for visual demonstration and the 12.7 mm hole was used for SNR calculation. d: CAD model of the phantom set up. The cavity was fixed inside a plastic jar and then placed on two 3D-printed supporters, allowing the jar to be set to the desired coil angle. e: Assembled phantom set up. The resolution plate was taped tightly under the cavity and then the cavity was fixed in a plastic jar. f: The plastic jar was filled with agar gel, and the coil was placed inside the cavity.

Germany: 50 Ω, 1.13 mm diameter, 0.22 mm inner conductor diameter, 20 cm length) connected the coil to a custom 3D printed circuit box located outside the body. This box housed the electrical pre-amplifier circuit, with adjustable components needed for tune and match. All of the electronics can be kept outside the body with only the coil loop and cable needing to be inserted endonasally. The coil assembly was tuned to a resonance frequency of 123.2 MHz (for 3T imaging) and impedance matched by adjusting the electrical components contained in the box [17]. The circuit was also designed to actively decouple the loop, without lumped element capacitors, during the transmit portion of the pulse sequence. The active detuning was accomplished by putting an inductor in parallel with the net capacitance of the coax cable during the transmit portion of the pulse sequence, detuning the inductive coil loop. Due to proprietary Siemens hardware, a custom built-in docking port was designed specifically for our assembly by author RH via an MCX connector.

C. COIL PERFORMANCE SIMULATION

Modeling of the MRI RF coils is an important step in coil design and development. A 3D coil model was developed in COMSOL® (COMSOLAB, Stockholm, Sweden) to study the magnetic field distributions of the coil. A circular loop coil with a 20 mm inner diameter and a trace width of 3 mm was set up in the frequency domain. The coil was assigned as Perfect Electric Conductor surface and the current flowing in the coil was set to 1 A. The sample properties in the simulation were set up according to the material properties of the agar-carrageenan gel [18]. For this finite element simulation, a maximum element size of 0.5 mm was used on the region of interest (ROI), and the simulated fields from the coil, $\boldsymbol{B_1}$ fields, at each vertex were imported into MATLAB (The MathWorks, Inc., Natick, Massachusetts, United States) for post-processing.

The simulated amplitude of the effective transverse field $B_{1xy\,effective}$ at the resonance frequency within the ROI was evaluated and then compared with the MRI scan results. The magnetic field components were simulated with the coil plane parallel to the B_0 field ($\theta = 0°$) (Fig. 2a), and then the amplitude of the effective transverse field at a certain rotation angle θ ($0° < \theta \leq 90°$) with respect to B_0 (Fig. 2b) was derived as:

$$B_{1y\,effective} = B_{1y} \cdot cos\theta - B_{1z} \cdot sin\theta \quad (1)$$

$$B_{1xy\,effective} = \sqrt{B_{1x}B^*_{1x} + B_{1y\,effective}B^*_{1y\,effective}} \quad (2)$$

where B_{1x}, B_{1y}, and B_{1z} are the magnetic field components for our RF receiving coil in x, y, z directions at $\theta = 0°$. B_{1x}, B_{1y}, and B_{1z} remain constant during the rotation.

D. PHANTOM DESIGN AND CONSTRUCTION

A 3D-printed phantom was designed and manufactured to roughly mimic the sphenoid sinus dimensions as an igloo-shaped configuration (Fig. 3a and 3b). A surrounding cylindrical jar (Fig. 3d) allowed for easy rotation of the assembly, effectively tilting the coil rotation angle relative to the B_0 field.

To assess imaging resolution, the five holes, ranging from 1 mm to 2.8 mm in diameter, were drilled into an acrylic plate (2.5 cm thick and 7.5 cm wide), which was attached under the igloo cavity (Fig. 3c). In addition, a center hole of 12.7 mm in diameter was drilled to provide sufficient volume for SNR measurements. The cavity and the resolution plate were then fixed inside a transparent cylindrical plastic jar, parallel to the jar wall (Fig. 3d and 3e). The plastic jar was chosen to have a similar size as a human head, 13 cm in diameter and 12 cm in height. The plastic jar was rested on a pair of 3D-printed supporters, so the jar was able to be rotated and set at the desired scan angle. The plastic jar, including the holes in the

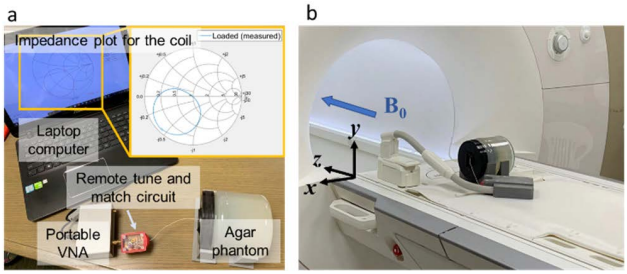

FIGURE 4. The tune and match process and the MRI scan experiment set up. a) A portable vector network analyzer (DG8SAQ VNWA 3, SDR-Kits, United Kingdom) was used for tune and match analysis after placing the coil inside the agar phantom. b) The tune and match box was connected to the pre-amplifier, and MRI scans were performed on the phantom.

resolution plate, was filled with agar gel, which consists of distilled water, 1% agar powder, 2% Kappa carrageenan, and 22 μmol/kg of gadolinium contrast (Fig. 3f) [19]. A portable vector network analyzer (VNA) was used to tune and match the coil after placing the coil inside the igloo cavity of the phantom (Fig. 4a).

E. MRI STUDIES USING THE PHANTOM

The tune and match of the miniature coil was performed by measuring the frequency response using the portable VNA for loaded and unloaded cases. Loaded S11 is measured with the phantom placed under the coil while unloaded S11 is measured with no phantom presented. For both loaded and unloaded cases, the miniature coil was tuned and matched to the resonance frequency of 123.2 MHz.

The T1/T2 value of the agar phantom was measured to be 1250/64 ms, with T1/T2 map sequences [20]. Standard resolution proton density Turbo Spin Echo (SD PD-TSE) sequences (Table 1) were used to compare our miniature coil with the commercial Siemens 20-channel HeadNeck coil, both quantitatively and qualitatively. Here we chose proton density because it is a direct measure of the maximum signal. The 2D SD PD-TSE sequence was scanned at 10 different coil rotation angles, ranging from 0 ° to 90°.

Given the expected higher SNR, we scanned the miniature coil with a 2D high-resolution proton density Turbo Spin Echo (HD PD-TSE) sequence (Table 1) at 0° and 60° coil angles. Images were reconstructed from the frequency data directly via inverse Fast Fourier Transform (iFFT). The HD PD-TSE scan was also performed on the commercial head coil using the same scan sequence. The commercial head coil images were sum-of-square combined after coil reduction.

F. SNR COMPUTATION

For each angle, SNR measurements for the single-channel custom coil were calculated from two repeated standard-resolution 2D PD-TSE scans. The region of interest (ROI) was divided into five cylindrical slices - each with 1 cm diameter and 3 mm thickness (Fig. 2) - inside the resolution plate center hole under the coil (Fig. 3d and 3e). When combined, the slices form a 1 cm diameter region 3 mm to

TABLE 1. The parameters for high-resolution 2D PD-weighted TSE sequence and standard-resolution 2D PD-TSE sequence.

	SD PD-TSE	HD PD-TSE
Echo time (ms)	9.1	14
Repetition time (ms)	3000	3000
Refocusing angle (degree)	160	160
Bandwidth (Hz/pixel)	250	250
Acquisition matrix size	320×320×15	320×320×35
Field of view (mm^3)	220×220×45	64×64×25
Resolution (mm^3)	0.7×0.7×3	0.2×0.2×0.7
Phase over sampling	0%	100%
Scan time (mm:ss)	03:09	06:21
Parallel imaging	No	No

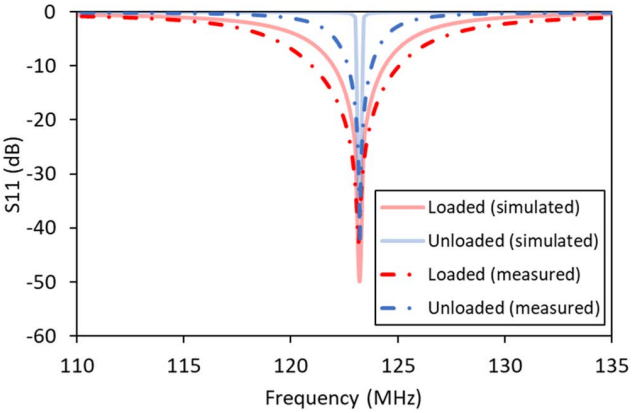

FIGURE 5. Comparison of S11 with and without the load measured with the VNA and simulated using COMSOL. The coil in both loaded and unloaded cases was tuned and matched to the resonance frequency.

18 mm away from the miniature coil. The defined ROI has a size comparable to a typical pituitary gland [21].

SNR measurements were calculated with methods described by Constantinides *et al.* for magnitude images of a single-coil array [22]. SNR was calculated as the ratio of signal and noise ($SNR = S/\sigma$). The signals were measured as the mean intensity within the ROI:

$$S = \frac{1}{N_{ROI}} \sum_{i=1}^{N_{ROI}} A_{ROI_i} \tag{3}$$

where N is the number of samples and A is the pixel intensity. The noise was measured as the background standard deviation on a signal-free region:

$$\sigma = \sqrt{\frac{1}{N_n} \sum_{i=1}^{N_n} \left(A_{n_i} - \overline{A_{n_i}}\right)^2} \tag{4}$$

In this experiment, the signal-free region was selected within the acrylic plastic part of the resolution block.

For the 20-channel commercial head coil, the SNR was calculated based on Kellman's method for root-sum-of-squares magnitude combining images, which is the gold standard for multi-channel phased array coils [23]. The scaled noise covariance matrix was calculated from averaging pixel

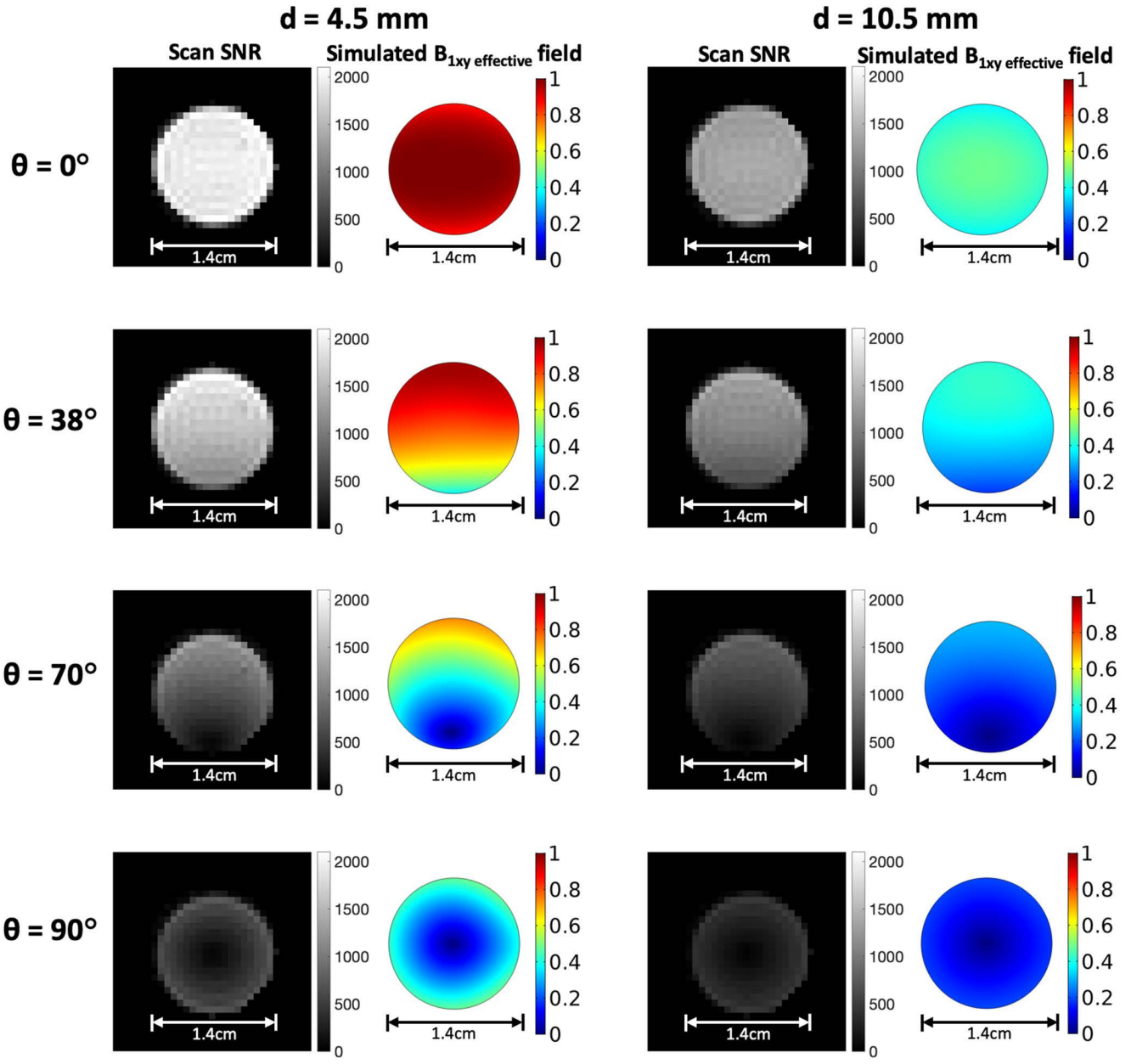

FIGURE 6. The scan (Table 1 line 1) signal SNR maps and normalized amplitude of the simulated effective transverse B_1 field distributions at $\theta = 0°$, 38°, 70° and 90°, respectively. d indicates the distance between the coil and the imaging plane. The imaging planes were selected to be parallel to the coil plane. Column 1&3: The SNR maps at the respective coil distances d and rotation angles θ. Column 2&4: The amplitudes of the simulated effective transverse B_1 field distributions at the central hole on the resolution Linear color scale indicates the level of the SNR and the normalized $B_{1xy\ effective}$. The simulation fields were normalized based on the maximum $B_{1xy\ effective}$ field at $d = 4.5$ mm.

SNR within ROI from two repeated standard-resolution 2D PD-TSE scans. Standard-resolution proton density Turbo Spin Echo (PD-TSE) MRI scans (Table 1 line 1) were performed on the phantom for SNR measurements for both miniature flexible coil and commercial head coil, and a coil simulation model was developed to characterize the performance of the coil. We plotted the SNR maps and the amplitudes of the simulated effective transverse B_1 field distributions for θ from 0° to 90°, at defined ROIs from 4.5 mm to 16.5 mm distance to the coil, shown in Fig. 2.

III. SIMULATION & EXPERIMENTAL RESULTS

A. S11 COMPARISON

The reflection coefficient S11 was recorded and then compared with the simulated S11 for the loaded and unloaded cases (Fig. 5). The simulated S11 generally agrees with the measured S11. The quality factor Q-factor can be approximated as the ratio of the resonant frequency (f_0) to the 3dB bandwidth ($\Delta f_{3\text{dB}}$) [24]. The simulated quality factors for the loaded case and the unloaded case are found to be $Q^{sim}_{loaded} = 16.88$, $Q^{sim}_{unloaded} = 308$. And the measured quality

factors are $Q^{mea}_{loaded} = 11.18$, $Q^{mea}_{unloaded} = 36.29$. The lower Q-factors from the measurement are likely to be the result of the environment loss that was not included in the simulation. A common measure for sensitivity to loading is the ratio between the unloaded Q-factor and loaded Q-factor [25], [26]. The measured Q-ratio is found to be $Q^{mea}_{ratio} = 3.25$ and the simulated Q-ratio is $Q^{sim}_{ratio} = 18.25$. A Q-ratio that is larger than 2 indicates that the sample noise dominates the coil noise [11].

B. IN-PLANE SNR MAP

Phantom scan in-plane SNR maps are shown in Fig. 6. The imaging planes were selected parallel to the coil surface at 4.5 mm and 10.5 mm below the coil, as a zoom-in shot on the resolution plate. The amplitudes of the simulated effective transverse B_1 field distributions at the same coil depth distance and rotation angles as the SNR maps are also shown in Fig. 6. In the simulation, the in-plane effective field amplitudes were normalized based on the maximum $B_{1xy\,effective}$ field at 4.5 mm below the coil.

As the coil angle increases, the overall SNR and the amplitude of the $B_{1xy\,effective}$ within the ROI decreases. Because of the circular shape of the small coil, the magnetic field from the coil is not uniform, and dead spots, where $B_{1xy\,effective}$ drops to zero, were observed in the in-plane results. When the rotation angles increased from 0° to 90°, the dead spot gradually moved from the edge of the ROI to the center of the ROI in both experiment and simulation. The simulated field distributions qualitatively matched with the scan experiment SNR maps.

A comparison of the high-resolution PD-TSE image between the head coil image and the miniature coil images is shown in Fig. 7. Though the SNR decreases with increasing rotation angle, the phantom signal is still uniform at 60° coil angle, and the image SNR is high enough to clearly show the 1 mm hole on the resolution plate.

C. MEAN SNR VS. COIL DISTANCE & ROTATION ANGLE

The mean SNR of the ROI from the phantom scan with respect to distance from the coil and the rotation angles are shown in Fig. 8, and then compared with the normalized mean $B_{1xy\,effective}$ within the ROI from the simulation. We normalized the effective transverse field predicted by simulation at a single point ($\theta = 0°$ at 4.5 mm below the coil). By setting this one point equal to the experimentally measured SNR, we can see that the simulations of magnetic field amplitude track with the experimentally measured SNR, with an error of $1.1\% \pm 0.8\%$. The mean effective field at $\theta = 90°$ dropped to around 20% of the mean-field found at $\theta = 0°$ for all ROI depths. At $\theta = 0°$, the mean effective field at 16.5 mm slice was 23.1% of the mean effective field at 4.5 mm slice. For an ideal coil, at $\theta = 90°$, the coil magnetic field B_1 is parallel to the main field B_0, and the SNR is expected to drop to zero. However, in the real case, only the B_{1y} component of the coil field is parallel to B_0 at $\theta = 90°$ (Fig. 2b), and spins can still be excited by B_{1x} and B_{1z} components, providing a reduced but detectable signal. The mean SNR of the 20-channel commercial head coil based on Kellman's method was 99.5 (Fig. 8) [23], which was uniform across the ROI.

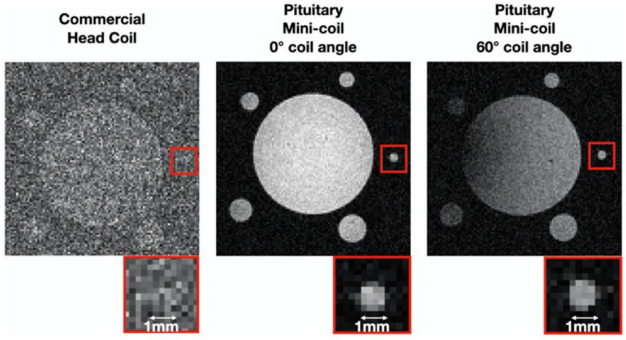

FIGURE 7. High-resolution PD-TSE image comparisons, using the commercial head coil (left), and the pituitary miniature flexible coil at $\theta = 0°$ (middle) and $\theta = 60°$ (right). The voxel size is 0.2 × 0.2 × 0.7 mm^3. Imaging planes were selected 1 cm from the coil. Images from miniature flexible coil are at the same window level, while the image from the commercial head coil is at its own window level for better visualization.

A Bland-Altman plot of two repeated standard-resolution PD-TSE scans, as shown in Fig. 9 was generated to show the inter-scan SNR consistencies. The 95% confidence interval indicated majority of repeated scans are within ±5% difference, which demonstrated the consistency and the repeatability of measure SNRs from phantom scans.

D. SURGICAL PLACEMENT RESULTS

An example hypothetical miniature coil surgical placement with the simulated SNR improvements in pituitary region is as shown in Fig.10. In the zoom-in view of the sphenoid sinus and the pituitary, the 2.6 cm miniature coil could be placed at a 30° angle with respect to B_0 field. Both coil placement and pituitary gland contour were drawn by an experienced neurosurgeon. The gradient line plots overlay represents the SNR improvement factors of our coil compared to the commercial head coil, which were estimated based on the mean SNR from the scan of the miniature coil and the commercial head coil. In this case, the pituitary gland enjoys a 12 to 19 times of SNR improvement at the region close to the coil, and at least 3 times of SNR improvement at the region further away.

IV. DISCUSSION

Our prototype coil, which was specifically designed for intra-operative imaging of the pituitary gland, achieved up to a 19-fold SNR improvement compared to a commercial head coil in this agar phantom study. Our ''worst-case-scenario,'' a rotation angle of 60 degrees and an ROI depth of 16.5 mm, still produced a 2-fold relative increase in SNR.

Re-tuning or matching is not necessary after the coil placement since the coil is tuned and matched after being placed in the sphenoid sinus. Since the coax cable is 20 cm long, it is short enough not to pick up any significant currents from the body coil during Tx. If the coax cable is made to

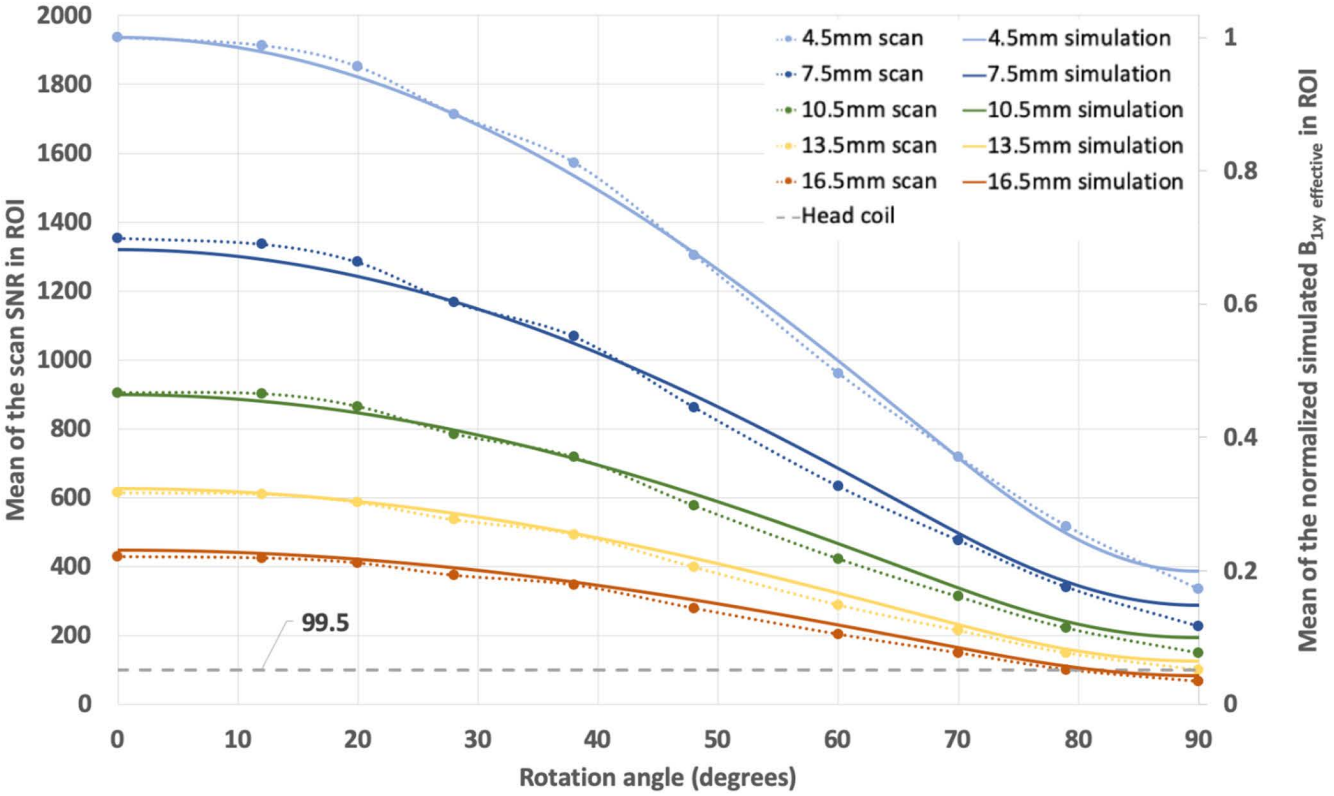

FIGURE 8. Mean SNR from the scan at various ROI depths and rotation angles, compared with the corresponding mean of the normalized effective transverse B_1 field from the simulation. The simulated fields were normalized to a single point, the mean $B_{1xy\ effective}$ at $\theta = 0°$ at 4.5 mm below the coil.

be longer than 20 cm, common mode current chokes could be placed along the length of the cable to impede the shield currents. This technique is supplemented with a balun on the pre-amplifier circuit board.

The increased SNR from the miniature coil enabled a markedly higher resolution imaging compared to the commercial head coil. The voxel size of the high-resolution sequence is approximately 1/50th of the standard-resolution. Because the SNR is proportional to the voxel size [27], our coil enabled a much-increased spatial resolution of that currently used with standard 3T imaging. At this reduced voxel size, the inadequate SNR associated with the commercial coil was demonstrable. To the contrary, our phantom study suggests that pituitary adenomas of 1 mm and smaller may be detectable using our custom miniature intrasphenoidal coil.

Multiple aspects of the electromagnetic behavior and performance of our custom coil were accurately simulated using a COMSOL multiphysics approach. The simulation of the effective magnetic field aligns with the experimentally measured SNR across a clinically relevant range of coil angles and distance, both in-plane pixel-wise and through-plane. The consistency of these two groups of simulation data and experiment data validates both the numerical simulation model and SNR experiments. The SNR from repeated scans also had little difference, demonstrating precise SNR measurements. The discrepancy remaining between the mean SNR curve and the simulation curve is likely attributable to errors in the imaging plane alignment. The imaging planes were selected manually on the scanner, and any mismatches in distance or rotation angle can create shifts in the SNR curves.

Validated with the phantom scan experiment, this coil simulation model is important in studying the interaction between the RF fields from the surface coil and the ROI or the phantom. As demonstrated in the surgical placement example, the simulated coil field can be potentially used to predict the SNR improvement of using the miniature coil compared to a commercial head coil. It will also allow us to simulate the performance of other surface coil designs with different diameters, geometries, resonance frequencies, and placement configurations, and therefore accelerate the development of improved coil designs for future phantom and cadaveric studies prior to clinical trials. Furthermore, we anticipate the simulation model will potentially enable selection of an optimal coil size and shape from a set of existing coil designs based on the specific anatomy of each patient.

An additional advantage of our design approach, which is modular and relatively easily adaptable, is that in theory the same relative multiplicative improvements in SNR would be achievable with higher field MRI scanners as they become clinically available. Prior research has qualitatively examined the image quality improvement for pituitary MRI with 7T scanners [3], [10]. Since a real-time tune and match is performed, the coil can be tuned to other resonance frequencies and thus suitable for any MRI scanner.

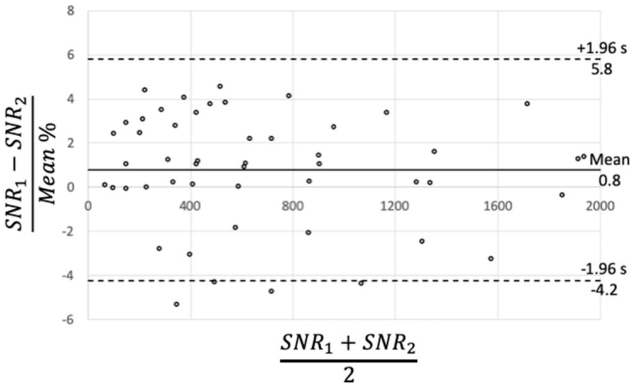

FIGURE 9. Bland-Altman plot for SNR of two repeated SD PD-TSE scans, SNR_1 and SNR_2. X-axis is the mean of the two scans, and Y-axis is the percentage difference.

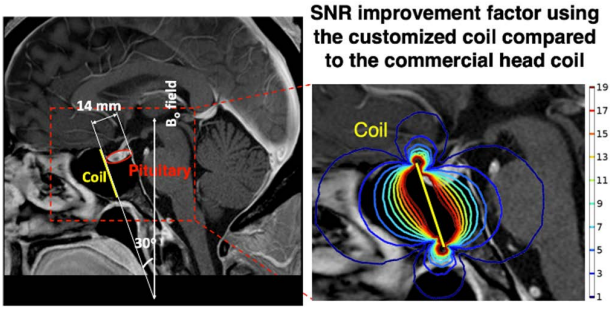

FIGURE 10. Coil surgical placement example on the retrospective patient image. SNR improvement using the miniature coil compared to a commercial head coil was estimated using the simulated effective field at $\theta = 30°$. The red ellipse indicates the location of the pituitary gland.

A. LIMITATIONS

"Dead spots" were found in the SNR maps and the simulated B_1 field distributions. The dead spots were observed at the locations where the coil field B_1 is parallel to the MRI main field B_0. At these locations, little or no spins were excited and thus, the signal dropped significantly. This low signal region is a common issue observed in MRI images when using the single loop coil and it limits the placement region of the coils. This limitation can be possibly circumvented by using coils with a transverse B_1 field at the center of the coil, such as the butterfly coils or figure-of-eight coils [14], [28].

We acknowledge that the coil design tested may be too large for patients with smaller sphenoid sinus cavities, as this cavity configuration and size varies between patients [2], [29]. Future coil designs with various shapes and dimensions can be customized to fit more patients. Further research on surgical placement with a larger patient database is necessary to optimize the future coil set design.

Although our phantom was designed to mimic human head and sphenoid sinus anatomy, it is not clear whether the results can be completely transferred to the clinical environment. The pituitary gland and surrounding tissues have non-uniform tissue contrast, which may cause Gibbs ringing artifact, susceptibility artifact, and chemical shifts artifact [30]–[32]. Future studies should involve cadaver or human patient studies for a definitive assessment of the miniature coil performance in the actual clinical environment.

The clinical application of our custom coil will require the ability to sterilize the intracavity portion and appropriate safety considerations. Specialty coatings and adhesives, such as Plasti Dip (Plasti Dip Int., Minneapolis, MN, USA), can be applied to make the coil waterproof and heat insulated to prevent RF-induced heating. For future coil coating, other conformal biocompatible materials like the Parylene C can be applied and hydrogen peroxide plasma can be potentially used for sterilization [33]–[36].

V. CONCLUSION

A miniature flexible coil has been developed, and its feasibility was validated using numerical simulations and experimental phantom. The proposed coil design can be surgically positioned in close proximity to the pituitary gland, which can provide a maximum of 19-fold SNR improvement compared to a commercial head coil within a region of interest in the agar phantom study. A 3D coil simulation model was cross-validated with the experimental scan results, where the simulation model can be used to develop and refine new coil designs with predicted SNR gains in future studies. This study showed the feasibility of the miniature coil for high-SNR MRI of pituitary microadenoma.

ACKNOWLEDGMENT

(Jiahao Lin and Siyuan Liu contributed equally to this work.)

REFERENCES

[1] J. Jagannathan, R. Smith, H. L. DeVroom, A. O. Vortmeyer, C. A. Stratakis, L. K. Nieman, and E. H. Oldfield, "Outcome of using the histological pseudocapsule as a surgical capsule in cushing disease," *J. Neurosurg.*, vol. 111, no. 3, pp. 531–539, Sep. 2009.

[2] O. Hamid, L. El Fiky, O. Hassan, A. Kotb, and S. El Fiky, "Anatomic variations of the sphenoid sinus and their impact on trans-sphenoid pituitary surgery," *Skull Base*, vol. 18, no. 1, pp. 9–15, Jan. 2008.

[3] A. A. J. de Rotte, A. G. van der Kolk, D. Rutgers, P. M. J. Zelissen, F. Visser, P. R. Luijten, and J. Hendrikse, "Feasibility of high-resolution pituitary MRI at 7.0 Tesla," *Eur. Radiol.*, vol. 24, no. 8, pp. 2005–2011, May 2014.

[4] M. C. R. Espagnet, L. Bangiyev, M. Haber, K. T. Block, J. Babb, V. Ruggiero, F. Boada, O. Gonen, and G. M. Fatterpekar, "High-resolution DCE-MRI of the pituitary gland using radialk-space acquisition with compressed sensing reconstruction," *Amer. J. Neuroradiol.*, vol. 36, no. 8, pp. 1444–1449, Aug. 2015.

[5] S. L. Tsai, E. Laffan, and S. Lawrence, "A retrospective review of pituitary MRI findings in children on growth hormone therapy," *Pediatric Radiol.*, vol. 42, no. 7, pp. 799–804, Jul. 2012.

[6] F. Castinetti, T. Graillon, H. Dufour, and T. Brue, "Letter to the editor: 'Why we should still treat by neurosurgery patients with cushing disease and a normal or inconclusive pituitary MRI,'" *J. Clin. Endocrinol. Metabolism*, vol. 104, no. 12, pp. 5791–5792, Dec. 2019.

[7] Y. Grober, H. Grober, M. Wintermark, J. A. Jane, and E. H. Oldfield, "Comparison of MRI techniques for detecting microadenomas in cushing's disease," *J. Neurosurgery*, vol. 128, no. 4, pp. 1051–1057, Apr. 2018.

[8] M. Varrassi, F. C. Bellisari, F. Bruno, P. Palumbo, R. Natella, N. Maggialetti, M. D. Filippo, E. D. Cesare, A. Barile, C. Masciocchi, F. Caranci, and A. Splendiani, "High-resolution magnetic resonance imaging at 3T of pituitary gland: Advantages and pitfalls," *Gland Surg.*, vol. 8, no. S3, pp. S208–S215, Sep. 2019.

[9] A. Yao, J. W. Rutland, G. Verma, A. Banihashemi, F. Padormo, N. M. Tsankova, B. N. Delman, R. K. Shrivastava, and P. Balchandani, "Pituitary adenoma consistency: Direct correlation of ultrahigh field 7T MRI with histopathological analysis," *Eur. J. Radiol.*, vol. 126, May 2020, Art. no. 108931.

[10] M. Law, "Erratum. Value of pituitary gland MRI at 7 T in cushing's disease and relationship to inferior petrosal sinus sampling: Case report," *J. Neurosurg.*, vol. 130, no. 2, p. 661, Feb. 2019.
[11] B. Gruber, M. Froeling, T. Leiner, and D. W. J. Klomp, "RF coils: A practical guide for nonphysicists," *J. Magn. Reson. Imag.*, vol. 48, no. 3, pp. 590–604, Sep. 2018.
[12] Y. Mazaheri, H. A. Vargas, G. Nyman, A. Shukla-Dave, O. Akin, and H. Hricak, "Diffusion-weighted MRI of the prostate at 3.0T: Comparison of endorectal coil (ERC) MRI and phased-array coil (PAC) MRI—The impact of SNR on ADC measurement," *Eur. J. Radiol.*, vol. 82, no. 10, pp. e515–e520, Oct. 2013.
[13] P. Chittiboina, S. L, Talagala, H. Merkle, J. E. Sarlls, B. K. Montgomery, M. G. Piazza, G. Scott, A. Ray-Chaudhury, R. R. Lonser, E. H. Oldfield, A. P. Koretsky, and J. A. Butman, "Endosphenoidal coil for intraoperative magnetic resonance imaging of the pituitary gland during transsphenoidal surgery," *J. Neurosurg.*, vol. 125, no. 6, pp. 1451–1459, Dec. 2016.
[14] M. Alfonsetti, V. Clementi, S. Iotti, G. Placidi, R. Lodi, B. Barbiroli, A. Sotgiu, and M. Alecci, "Versatile coil design and positioning of transverse-field RF surface coils for clinical 1.5-T MRI applications," *Magn. Reson. Mater. Phys., Biol. Med.*, vol. 18, no. 2, pp. 69–75, May 2005.
[15] O. Beuf, F. Pilleul, M. Armenean, G. Hadour, and H. Saint-Jalmes, "*In vivo* colon wall imaging using endoluminal coils: Feasibility study on rabbits," *J. Magn. Reson. Imag.*, vol. 20, no. 1, pp. 90–96, Jul. 2004.
[16] A. Magill and R. Gruetter, "Nested surface coils for multinuclear NMR," in *RF Coils for MRI*, 1st ed., J. T. Vaughan and J. R. Griffiths, Eds. Chichester, U.K.: Wiley, 2012, pp. 39–50.
[17] J. R. Hadley, L. Slusser, P. R. Merrill, E. Minalga, and L. D. Parker, "Remote tuning and matching of a non-resonant wire loop," in *Proc. ISMRM*, Paris, France, 2018, p. 1721.
[18] H. Kato, K. Yoshimura, M. Kuroda, A. Yoshida, K. Hanamoto, S. Kawasaki, K. Shibuya, Y. Yamamoto, M. Tsunoda, M. Takemoto, and Y. Hiraki, "Development of a phantom compatible for MRI and hyperthermia using carrageenan gel—Relationship between dielectric properties and NaCl concentration," *Int. J. Hyperthermia*, vol. 20, no. 5, pp. 529–538, Aug. 2004.
[19] K. Yoshimura, H. Kato, M. Kuroda, A. Yoshida, K. Hanamoto, A. Tanaka, M. Tsunoda, S. Kanazawa, K. Shibuya, S. Kawasaki, and Y. Hiraki, "Development of a tissue-equivalent MRI phantom using carrageenan gel," *Magn. Reson. Med.*, vol. 50, no. 5, pp. 1011–1017, Nov. 2003.
[20] D. R. Messroghli, A. Radjenovic, S. Kozerke, D. M. Higgins, M. U. Sivananthan, and J. P. Ridgway, "Modified look-locker inversion recovery (MOLLI) for high-resolution T1 mapping of the heart," *Magn. Reson. Med.*, vol. 52, no. 1, pp. 141–146, 2004.
[21] A. P. Amar and M. H. Weiss, "Pituitary anatomy and physiology," *Neurosurg. Clinics North Amer.*, vol. 14, no. 1, p. 11–23, 2003.
[22] C. D. Constantinides, E. Atalar, and E. R. McVeigh, "Signal-to-noise measurements in magnitude images from NMR phased arrays," *Magn. Reson. Med.*, vol. 38, no. 5, pp. 852–857, 1997.
[23] P. Kellman and E. R. McVeigh, "Image reconstruction in SNR units: A general method for SNR measurement," *Magn. Reson. Med.*, vol. 54, no. 6, pp. 1439–1447, 2005.
[24] S. Solis-Najera, G. Cuellar, R. Wang, D. Tomasi, and A. Rodriguez, "Transceiver 4-leg birdcage for high field MRI: Knee imaging," *Revista Mexicana de Física*, vol. 54, no. 3, pp. 215–221, 2009.
[25] G. Giovannetti, R. Francesconi, L. Landini, M. F. Santarelli, V. Positano, V. Viti, and A. Benassi, "Conductor geometry and capacitor quality for performance optimization of low-frequency birdcage coils," *Concepts Magn. Reson.*, vol. 20B, no. 1, pp. 9–16, 2004.
[26] D. Zhang and Y. Rahmat-Samii, "A novel flexible electrotextile 3T MRI RF coil array for carotid artery imaging: Design, characterization, and prototyping," *IEEE Trans. Antennas Propag.*, vol. 67, no. 8, pp. 5115–5125, Aug. 2019.
[27] A. Macovski, "Noise in MRI," *Magn. Reson. Med.*, vol. 36, no. 3, pp. 494–497, Sep. 1996.
[28] A. Kumar and P. A. Bottomley, "Optimized quadrature surface coil designs," *Magn. Reson. Mater. Phys., Biol. Med.*, vol. 21, nos. 1–2, pp. 41–52, Mar. 2008.
[29] N. Wiebracht and L. Zimmer, "Complex anatomy of the sphenoid sinus: A radiographic study and literature review," *J. Neurological Surg. B, Skull Base*, vol. 75, no. 6, pp. 378–382, May 2014.
[30] R. Archibald and A. Gelb, "A method to reduce the Gibbs ringing artifact in MRI scans while keeping tissue boundary integrity," *IEEE Trans. Med. Imag.*, vol. 21, no. 4, pp. 305–319, Apr. 2002.
[31] R. C. Smith, R. C. Lange, and S. M. McCarthy, "Chemical shift artifact: Dependence on shape and orientation of the lipid-water interface," *Radiology*, vol. 181, no. 1, pp. 225–229, Oct. 1991.
[32] O. Dietrich, M. F. Reiser, and S. O. Schoenberg, "Artifacts in 3-T MRI: Physical background and reduction strategies," *Eur. J. Radiol.*, vol. 65, no. 1, pp. 29–35, Jan. 2008.
[33] S. E. Solis, G. Cuellar, R. L. Wang, D. Tomasi, and A. O. Rodriguez, "A compact parylene-coated WLAN flexible antenna for implantable electronics," *IEEE Antennas Wireless Propag. Lett.*, vol. 15, pp. 1382–1385, 2016.
[34] N. Beshchasna, B. Adolphi, S. Granovsky, M. Braunschweig, W. Schneider, J. Uhlemann, and K.-J. Wolter, "Influence of artificial body fluids and medical sterilization procedures on chemical stability of parylene C," in *Proc. 60th Electron. Compon. Technol. Conf. (ECTC)*, 2010, pp. 1846–1852.
[35] B. J. Kim, W. Jin, A. Baldwin, L. Yu, E. Christian, M. D. Krieger, J. G. McComb, and E. Meng, "Parylene MEMS patency sensor for assessment of hydrocephalus shunt obstruction," *Biomed. Microdevices*, vol. 18, no. 5, p. 87, Oct. 2016.
[36] D. W. J. Perry, D. B. Grayden, R. K. Shepherd, and J. B. Fallon, "A fully implantable rodent neural stimulator," *J. Neural Eng.*, vol. 9, no. 1, Feb. 2012, Art. no. 014001.

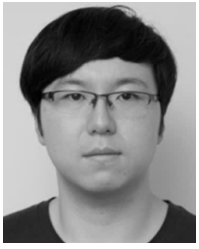

JIAHAO LIN (Member, IEEE) received the B.S. degree in electrical engineering and the M.S. degree in electrical and computer engineering from the University of California at Los Angeles (UCLA), USA, in 2014 and 2016, respectively, where he is currently pursuing the Ph.D. degree in electrical and computer engineering. His current research interest includes high-resolution MRI in various applications.

SIYUAN LIU received the B.S. degree in electrical engineering and the M.S. degree in electrical and computer engineering from the University of California at Los Angeles (UCLA), USA, in 2017 and 2019, respectively, with a focus on applications of electromagnetic waves, where she is currently pursuing the Ph.D. degree in physical and wave electronics area. Her current research interests include biomedical applications of electromagnetic waves and electromagnetics modeling and simulation.

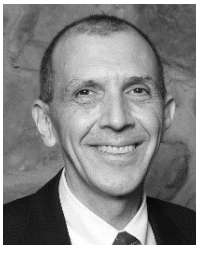

MARVIN BERGSNEIDER received the B.S. degree in electrical engineering from The University of Arizona, Tucson, in 1983, and the M.D. degree from the College of Medicine, The University of Arizona, in 1987.

He completed his neurosurgical residency training at the University of California at Los Angeles (UCLA), where he joined the faculty in 1994, and is currently a Professor of neurosurgery and a Faculty Member of the UCLA Biomedical Engineering Interdepartmental Program. His current research interests include modeling of intracranial pressure dynamics and advanced imaging techniques.

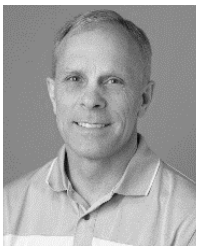

J. ROCK HADLEY received the B.S., M.E., and Ph.D. degrees in electrical engineering from The University of Utah, Salt Lake City, in 1992, 1996, and 2006, respectively. In 1996, he joined the Medical Imaging Research Laboratory, Department of Radiology, The University of Utah, where he is currently an Assistant Professor with the Department of Radiology and Imaging Sciences, managing the Radio Frequency (RF) Coil Laboratory. His research primarily focuses on the development of novel medical imaging hardware that advances medical imaging technology and improves signal-to-noise ratio in unique and complex magnetic resonance imaging (MRI) experiments. In particular, his RF Coil Laboratory specializes in designing, construction, and testing of specific application support hardware and imaging coils that enable or improve medical imaging research for a wide range of different animal and human studies. His RF coil expertise includes the design of dedicated MRI coils for standard anatomical imaging of specific anatomy to spectroscopy and complex high intensity focused ultrasound imaging applications.

GIYARPURAM N. PRASHANT received the M.D. degree from the Baylor College of Medicine, in 2014. He completed his residency in neurological surgery at the David Geffen School of Medicine/UCLA Medical Center, UCLA, from 2014 to 2021. He is currently a fellow with Thomas Jefferson University, specialized in skull base surgery.

SOPHIE PEETERS received the M.D. degree from the Medical School, The University of Texas Southwestern Medical Center, in 2017. She started her residency in neurological surgery at the David Geffen School of Medicine/UCLA Medical Center, UCLA, in 2017. She was a recipient of the AANS 2nd Place Tumor Electronic Poster Award in 2016 and the P. E. O. Scholar Award Finalist.

ROBERT N. CANDLER (Senior Member, IEEE) received the B.S. degree in electrical engineering from Auburn University, in 2000, and the M.S. and Ph.D. degrees in electrical engineering from Stanford University, in 2002 and 2006, respectively, as a National Defense Science and Engineering Graduate Fellow and an NSF Fellow. He is currently a Professor of electrical and computer engineering with the University of California at Los Angeles (UCLA), with joint appointments at the Department of Mechanical and Aerospace Engineering and the California NanoSystems Institute. Before coming to UCLA, he spent three years in corporate Research and Development with the Bosch Research and Technology Center. His research interests include micro- and nano-electromechanical systems (MEMS/NEMS), including microscale magnetic devices for electron beam manipulation, the fundamental behavior of MEMS/NEMS devices, miniature medical devices, and multiferroics. He has authored or coauthored more than 100 papers in major conferences and journals, five book chapters, and six patents. He is a Senior Member of the National Academy of Inventors and a fellow of the American Institute for Medical and Biological Engineering. He was a recipient of the Young Investigator Award from the Army Research Office and the Northrop Grumman Excellence in Teaching Award from the Henry Samueli School of Engineering and Applied Science, UCLA, both in 2012. He was also a recipient of the NSF CAREER Award in 2014 and the Lockheed Martin Excellence in Teaching Award in 2020.

KYUNGHYUN SUNG (Member, IEEE) received the Ph.D. degree in electrical engineering from the University of Southern California, Los Angeles, in 2008. From 2008 to 2012, he completed his postdoctoral training at the Department of Radiology, Stanford University. In 2012, he joined the Department of Radiological Sciences, University of California at Los Angeles (UCLA), Los Angeles, where he is currently an Associate Professor of radiology and his research primarily focuses on the development of novel medical imaging methods and artificial intelligence using magnetic resonance imaging (MRI). In particular, his research group is currently focused on developing advanced deep learning algorithms and quantitative MRI techniques for early diagnosis, treatment guidance, and therapeutic response assessment for oncologic applications. Such developments can offer more robust and reproducible measures of biologic markers associated with human cancers.